Nanoscale Horizons

ROYAL SOCIETY OF CHEMISTRY

COMMUNICATION

View Article Online
View Journal | View Issue

Cite this: *Nanoscale Horiz.*, 2026, 11, 243

Received 16th August 2025,
Accepted 29th October 2025

DOI: 10.1039/d5nh00588d

rsc.li/nanoscale-horizons

Spermine-responsive supramolecular DNA nanogels loaded with dual drugs for potential combined cancer therapy

Zongze Duan, Xiang Yu, Pengwei Jiang, Shuhao Wang, Junling Chen, Zhiyong Zhao * and Simin Liu *

The construction of nano-drug carriers based on deoxyribonucleic acid (DNA) has demonstrated significant therapeutic potential. Similarly, supramolecular therapeutic systems utilizing host–guest interactions have emerged as promising in nanomedicine. Building upon these approaches, we designed a size-controllable, multi-responsive supramolecular DNA nanogel (SDN) based on host–guest recognition for dual-drug co-delivery in cancer combination therapy. The nanogel incorporates doxorubicin (DOX, a chemotherapeutic agent) and methylene blue (MB, a photosensitizer). The assembly of SDN is driven by cucurbit[8]uril (CB[8]), which selectively binds two MB molecules—one from each of two Y-shaped DNA building blocks—forming a 1:2 host–guest complex that crosslinks the structures into a nanogel network. Meanwhile, the double-stranded DNA scaffold efficiently encapsulates DOX *via* intercalation, enabling SDN@DOX to co-deliver both drugs in a precisely controlled ratio. Notably, MB's photodynamic activity is initially suppressed upon CB[8] binding. However, upon cellular uptake, SDN@DOX responds to overexpressed spermine or specific peptide sequences in the tumor microenvironment, triggering MB release and restoring its photodynamic function. Concurrently, DNase I-mediated DNA degradation liberates DOX, enabling synergistic chemo-photodynamic therapy (PDT). *In vitro* studies confirmed that SDN@DOX enhances reactive oxygen species (ROS) generation in cancer cells and achieves superior therapeutic efficacy through combined PDT and chemotherapy. This stimuli-responsive, dual-drug delivery system offers a potentially robust and controllable platform for precision cancer treatment.

New concepts

We present a universal strategy for constructing supramolecular DNA nanogels (SDNs) through cucurbit[8]uril (CB[8])-mediated host–guest interactions with homo-guest molecules. Specifically, CB[8] selectively binds two methylene blue (MB) molecules—each positioned at the terminus of Y-shaped DNA building blocks—forming a stable 1:2 host–guest complex that drives the hierarchical assembly of SDNs. This supramolecular approach complements conventional DNA nanogel fabrication techniques, such as base pairing, enzymatic ligation, rolling circle amplification, or hybridization, offering distinct advantages. The system achieves enhanced stability through high-affinity CB[8]·MB host–guest interactions. It enables stimuli-responsive drug release: while CB[8] initially quenches MB's photodynamic activity, competitive displacement by spermine or the FGG peptide restores MB's function while reducing off-target toxicity. The design retains all advantages of DNA nanogels, including precise size control, biocompatibility, and programmable functionalization. Furthermore, the double-stranded DNA framework of SDNs enables efficient loading of chemotherapeutics doxorubicin (DOX) for combined therapy. Crucially, this platform is highly versatile: by modifying guest molecules, SDNs can be tailored for diverse biomedical applications, from tumor-selective drug delivery to diagnostic nanosensing. We anticipate this strategy will advance the development of smart DNA-based nanomedicines, bridging supramolecular chemistry and functional biomaterials for precision therapeutics.

Introduction

Cancer, as one of the leading causes of death worldwide, poses a serious threat to human life and health. Commonly used clinical cancer treatment methods include chemotherapy, radiotherapy and surgical treatment, which often have some unavoidable side effects and cause harm to patients' physical and mental health.[1] To overcome the limitations of traditional therapies, some new treatment methods such as photodynamic therapy (PDT),[2] photothermal therapy (PTT)[3] and chemodynamic therapy (CDT)[4] have been developed, aiming to improve treatment efficacy and reduce adverse reactions to patients. These methods facilitate the delivery of therapeutic agents to target sites, where they can be activated by external energy input or intracellular stimuli, thereby significantly reducing damage to normal cells. Moreover, compared with the single-drug therapy, the simultaneous delivery of two or more drugs often exhibits a synergistic effect and reduces cancer cell drug

Key Laboratory of Hubei Province for Coal Conversion and New Carbon Materials, School of Chemistry and Chemical Engineering, Wuhan University of Science and Technology, Wuhan 430081, China. E-mail: zhaozhiyong@wust.edu.cn, liusimin@wust.edu.cn

resistance.[5,6] To address this need, diverse nanocarriers have been developed and improved for the co-delivery of combination drugs. These nanocarriers include liposomes,[7] inorganic nanoparticles especially upconversion nanoparticles,[8–10] polymer nanoparticles[11–14] and nanogels,[15,16] which help to achieve synergistic therapy. Among these nanocarriers, nanogels have been extensively studied due to their controllable size and tunable internal network architectures. These nanostructures are typically synthesized *via* either physical cross-linking of polymeric chains or chemical polymerization of monomers.

Deoxyribonucleic acid (DNA), as an endogenous biomacromolecule, has been utilized as a building block to construct different nanomaterials in drug delivery systems (DDSs).[17–20] Some pristine DNA nanostructures, fabricated from DNA origami[21] technology or a DNA tile[22] approach, have been developed and applied in drug delivery and biological imaging fields.[23–25] On the one hand, its addressable surface can precisely load the required cargos, such as aptamers and gene drugs through DNA hybridization; on the other hand, the DNA nanostructures can envelop hydrophobic drug molecules by an intercalation process or electrostatic interaction. Other kinds of DNA nanomaterials are assembled from DNA amphiphiles, which are composed of DNA strands and hydrophobic molecules. Due to the addition of DNA, DNA amphiphilic assemblies can have more biological functions.[26] In recent years, increased research on DNA nanogels has emerged.[27–30] These three-dimensional network structures exhibit good biocompatibility, controllable biodegradability, and responsiveness to various stimuli. Their easy-to-modify property enables them to be combined with other functional molecules to form composite DNA nanogels, greatly expanding their application.[31]

In recent years, supramolecular therapeutic systems based on host–guest recognition have emerged as a promising addition to nanomedicine.[32–34] Cucurbit[*n*]urils (CB[*n*]s), as the fourth-generation supramolecular host molecules, have significant potential for application in the field of supramolecular therapy. Due to its unique hydrophobic cavity and carbonyl port, CB[*n*]s can selectively recognize one or more guest molecules and form host–guest inclusion complexes with high affinity.[35–37] For instance, CB[7] can recognize some drug molecules, such as cisplatin[38] and oxaliplatin,[39] thereby enhancing the solubility and stability of these drugs. CB[8], with its relatively larger cavity, can even recognize two guest molecules. This unique property facilitates the construction of supramolecular nanomaterials. Importantly, this recognition process is non-covalent, dynamic, and reversible, which enables it to respond to external stimuli, especially some abnormal conditions at tumor sites.[40]

Herein, we designed and prepared spermine-responsive dual-drug-loaded supramolecular DNA nanogels (SDN@DOX) with combined photodynamic and chemotherapeutic properties by integrating both a supramolecular therapeutic strategy and DNA assembly approach (Scheme 1). Briefly, the SDN was synthesized *via* host–guest interactions between methylene blue (MB), modified at the termini of Y-type DNA structures, and the macrocyclic host molecule CB[8]. MB is not only a guest

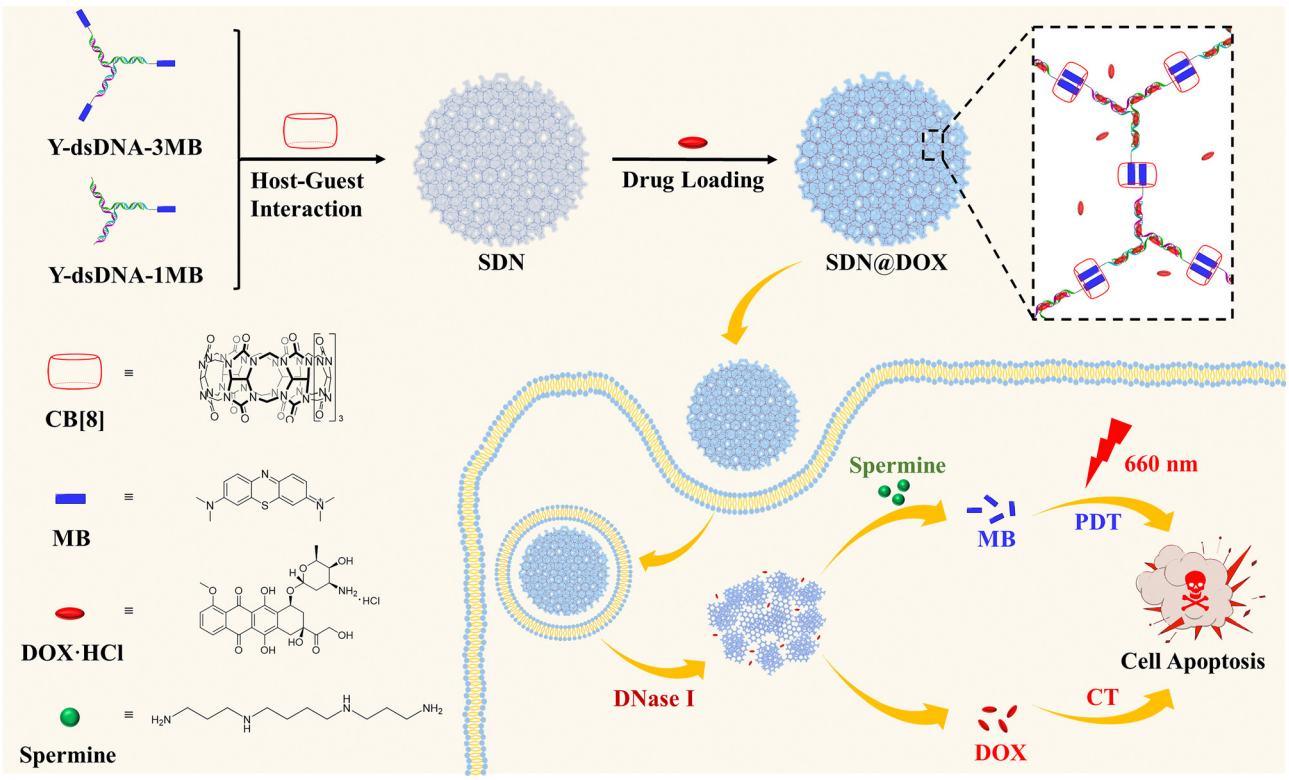

Scheme 1 Preparation of spermine-responsive SDN@DOX for combined photodynamic and chemotherapy.

molecule, but a photosensitizer for photodynamic therapy. Doxorubicin (DOX) was incorporated during the preparation process to achieve dual-drug loading supramolecular DNA nanogels (SDN@DOX). By adjusting the concentration of Y-type DNA, the formed SDN with sizes ranging from 50 to 500 nm can be obtained. In PBS solution and physiological environments, SDN@DOX exhibited excellent stability. Upon cellular uptake by cancer cells, MB could be released from the cavity of CB[8] in response to the overexpressed spermine in cancer cells, generating reactive oxygen species (ROS) under laser irradiation for photodynamic therapy (PDT).[41] Simultaneously, under the action of DNase I, SDN@DOX disassembled, releasing DOX for combined chemotherapy. All of the cell uptake, ROS generation, cytotoxicity and apoptosis tests suggested that the dual-drug-loaded supramolecular DNA nanogels could achieve the combined photodynamic and chemotherapy.

Results and discussion

Preparation and characterization of SDN

The assembly process of SDN is illustrated in Scheme 1. Two distinct Y-shaped DNA structures, namely Y-dsDNA-3MB (Y-3MB) and Y-dsDNA-1MB (Y-1MB), were synthesized *via* annealing processes at 90 °C for 5 minutes. Y-3M was formed from three single strands modified with MB, DNA ssDNA1-MB, ssDNA2-MB and ssDNA3-MB. The detailed sequences are listed at Table S1. Subsequently, the gelation behavior of SDN was investigated by varying the concentrations of these two components while maintaining a constant molar ratio of 3 : 1 between Y-3MB and Y-1MB (Table S2). In the mixed solution of Y-3MB and Y-1MB, add a CB[8] solution at 10 times the equivalent of Y-1MB (so that the molar ratio of MB to CB[8] in the system is 2 : 1). Then, the mixed solution was sonicated for 2 minutes and left at 4 °C overnight. SDN was characterized using transmission electron microscopy (TEM) and dynamic light scattering (DLS). When the concentration of Y-3M was 0.45 μM, 0.90 μM and 1.80 μM respectively, the average sizes of SDN were 54.04 nm, 123.51 nm, and 435.21 nm, respectively (Fig. 1a–c and Fig. S1). The DLS data are consistent with the TEM results (Fig. 1d). These results indicate that the size of SDN becomes larger as the concentrations of the two assembled modules increase during the gelation stage. These findings confirmed that the size of SDN can be effectively controlled by adjusting the assembly concentrations of Y-3MB and Y-1MB. Considering the subsequent cell experiments, the SDN with 123.51 nm were selected for further investigation.

Gelation mechanism of SDN

MB, a phenothiazine derivative, has the capability to intercalate into the double strand DNA helix with a binding constant of 0.61×10^5 M^{-1}.[42] But due to the high affinity between CB[8] and two MB molecules (the binding constant $K_a = 11 \times 10^{16}$ M^{-2}),

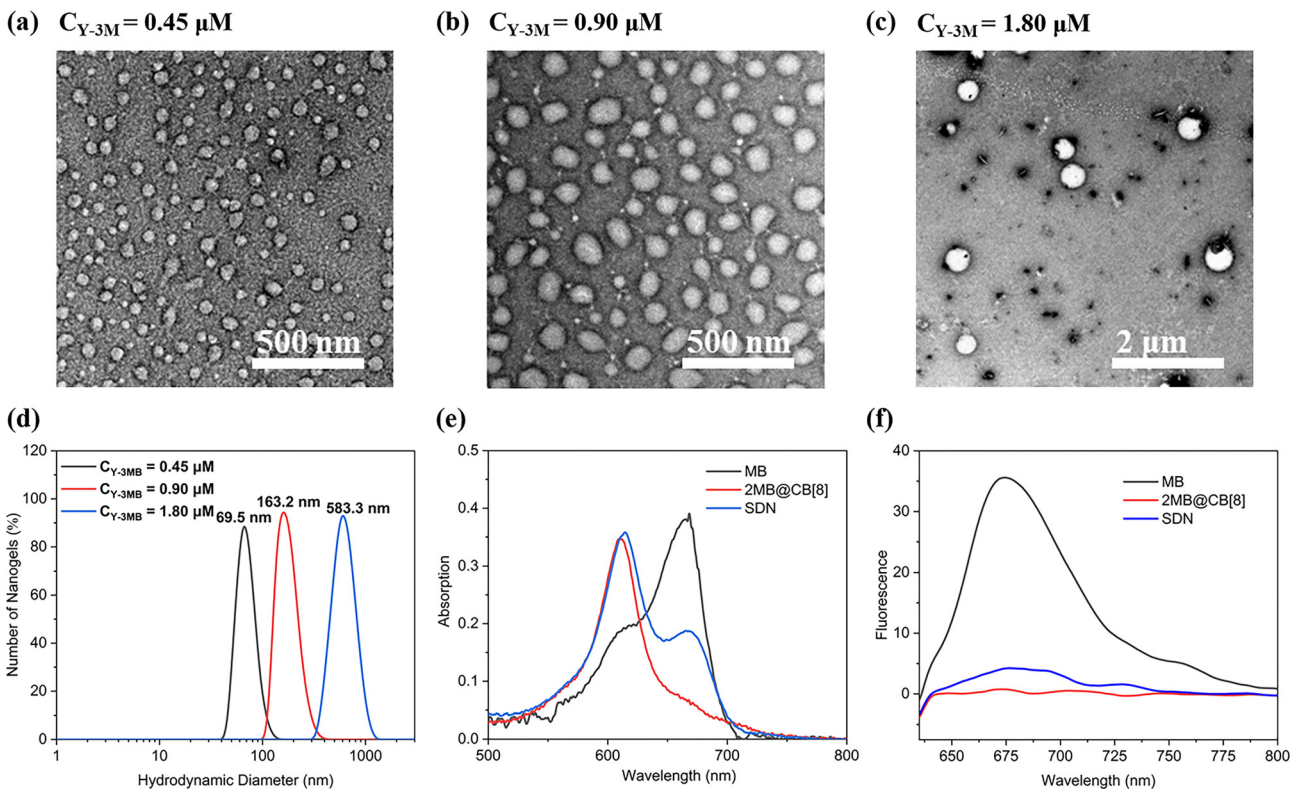

Fig. 1 (a)–(c) TEM images of SDN at different Y-3M concentrations, the molar ratio of Y-3MB and Y-1MB was 3 : 1, and the concentrations of Y-3MB were 0.45 μM (a), 0.90 μM (b) and 1.80 μM (c), respectively; (d) DLS data of SDN at different concentrations; (e) UV absorption spectra of MB, 2MB@CB[8] and SDN; and (f) fluorescence spectra of MB, 2MB@CB[8] and SDN.

CB[8] can recognize two MB molecules to form a 1 : 2 host–guest complex.[43] Here UV test and fluorescence spectroscopy analyses were conducted to study the gelation mechanism. As illustrated in Fig. 1e, free MB exhibits a characteristic absorption peak at 660 nm. Upon recognition by CB[8], the absorption at 660 nm disappeared, while a new characteristic absorption peak emerges at 600 nm, which indicated the formation of the 2MB@CB[8] complex. In the supramolecular DNA nanogels, the absorption at 660 nm significantly decreased, and the peak of 660 nm was similar with that of the 2MB@CB[8] complex. This result indicates that the host–guest interaction between CB[8] and MB molecules leads to the formation of supramolecular DNA nanogels. Furthermore, a strong fluorescence emission of MB molecules at 670 nm was observed (Fig. 1f). After host–guest interaction between CB[8] and MB molecules, the fluorescence was quenched. And the SDN system showed a similar result, which further proves the importance of host–guest interactions for the formation of supramolecular DNA nanogels.[44]

In vitro multiple responsiveness of SDN and reactive oxygen species (ROS) generation

One critical feature of supramolecular therapeutic strategy is the stimulus-responsiveness. According to the previous reports,[37,45] CB[*n*]s, as host molecules, exhibit high affinity for certain specific amino acids (with N-terminal aromatic groups), peptides and proteins. Here choose the FGG peptide served as a model system in our study, due to its high binding constant of 1.5×10^{11} M^{-2}. This suggests that the FGG peptides could be used as a competitive guest, and lead to the dissociation of the 2MB@CB[8] complex. As FGG peptide increased from 3 μM to 600 μM, the characteristic UV absorption peak of SDN at 610 nm gradually reduced, while the absorption peak of free MB at 665 nm correspondingly strengthened (Fig. 2a and Fig. S2a). These results indicate that FGG peptide could effectively compete with MB for the cavity of CB[8], thereby causing the release of MB from the host–guest complex. It also proved the good stimulus-responsive drug release behavior of the SDN.

To further simulate the controlled drug release ability of the SDN system within tumor cells, spermine was introduced as another competitive guest molecule in the experiment. Spermine is a kind of natural polyamine molecule that is abnormally highly expressed in various types of cancer cells (typically, its concentration in cancer cells reaches millimolar levels).[46–48] More importantly, spermine could form a stable host–guest complex with CB[8]. As shown in Fig. 2b, with the addition of spermine from 3 μM to 6 mM, the peak of 665 nm was gradually increased. The results demonstrated that high spermine concentrations triggered the release of MB from the CB[8] cavity (Fig. S2b), confirming the SDN system's stimulus-responsive behavior under tumor-mimicking conditions. Compared with the addition of FGG, spermine addition caused a slower MB release, which showed the potential for drug sustained-release application.

In addition, the morphology change of SDN after the responsiveness was investigated by DLS and TEM. As shown in Fig. 2c, after co-incubation with FGG peptides for 1 hour, the

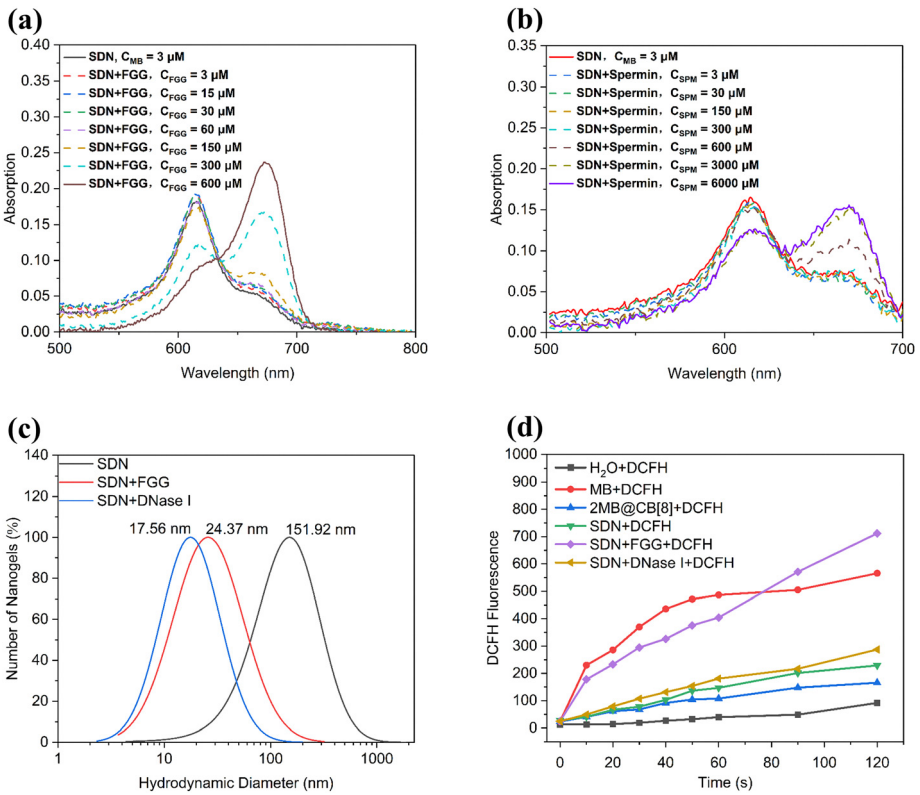

Fig. 2 UV characteristic absorption peaks of SDN with the addition of different concentrations of FGG peptides (a) and spermine (b) after incubation at 37 °C for 1 h; (c) DLS data of SDN after treating with FGG peptides (600 μM) and DNase I (50 U mL^{-1}) for 1 h; (f) *in vitro* ROS generation situation.

size of SDN significantly changed from 152 nm to approximately 24 nm, which was consistent with the TEM data (Fig. S3a). This significant size change indicates that the introduction of FGG peptides lead to the dissociation of SDN and the release of drug MB. This further confirmed the competitive guest responsiveness of the SDN system.

Meanwhile, the DNA enzyme-responsiveness of SDN system was also studied. After adding DNase I for 1 h, the size was decreased to 18 nm (Fig. 2c), which was also proved by TEM test (Fig. S3b). These results demonstrated that the DNase I could disassemble the supramolecular DNA nanogel, and probably induce the drugs enveloped in double-strand DNA structures to be released.

Furthermore, the ROS generation capacity of SDN was evaluated using DCFH. As shown in Fig. 2d and Fig. S4, MB, a photosensitizer, could generate reactive oxygen species (ROS). After being recognized by CB[8] in the 2MB@CB[8], SDN and SDN + DNase I system, the ROS generation capacity was significantly reduced, which suggested that the 2MB@CB[8] complex was formed in the SDN system. Furthermore, DNase I just disrupted the nanogel but could not allow MB release due to the host–guest interaction. But when FGG peptides were added into the SDN system, the ROS generation capacity of SDN nearly returned to the level of free MB, demonstrating that SDN has good responsiveness and controllability.

The loading and release of DOX and the stability of SDN@DOX

The DOX loading method for SDN was based on our previous study.[49] The drug loading capacity was calculated by determining the standard fluorescence curve of DOX and detecting the DOX concentration in the supernatant of SDN after high-speed centrifugation (Fig. S5). When the DOX concentration was within the range of 5–24 μg mL^{-1}, the encapsulation efficiency could be maintained at approximately 95% (Fig. 3a). In Fig. S6, the SDN itself exhibited a negative surface charge of −11.12 mV. After loading with DOX hydrochloride, which carries a positive charge, the zeta potential of SDN@DOX increased to −9.34 mV. This change was consistent with the successful incorporation of the positively charged DOX into the SDN. From a biological perspective, the moderately negative surface charge of the nanogel is advantageous. It contributes to the colloidal stability of the system in physiological environments and may help reduce nonspecific interactions with negatively charged cell membranes under normal conditions. So the dual-drug coloaded supramolecular DNA nanogel SDN@DOX was achieved. Subsequently, the drug release behavior of SDN@DOX was investigated (Fig. 3b). After adding 50 U mL^{-1} DNase I for 40 min, DOX in the SDN@DOX system was almost completely released (about 100%), which was calculated through the DOX concentration-standard curve established based on the ultraviolet absorption (Fig. S7). In addition, the drug release was less than 15% within 24 h in PBS buffer at pH 7.4. And when SDN@DOX was incubated with DMEM medium containing 10% fetal bovine serum for 3 h, the release of DOX was less than 40% (Fig. S8). These results indicated the controlled drug release of the SDN@DOX system under DNase I triggered conditions. Meanwhile, the stability of SDN@DOX was investigated. The nanogel SDN@DOX system was incubated in PBS buffer (pH 7.4) for 7 days,

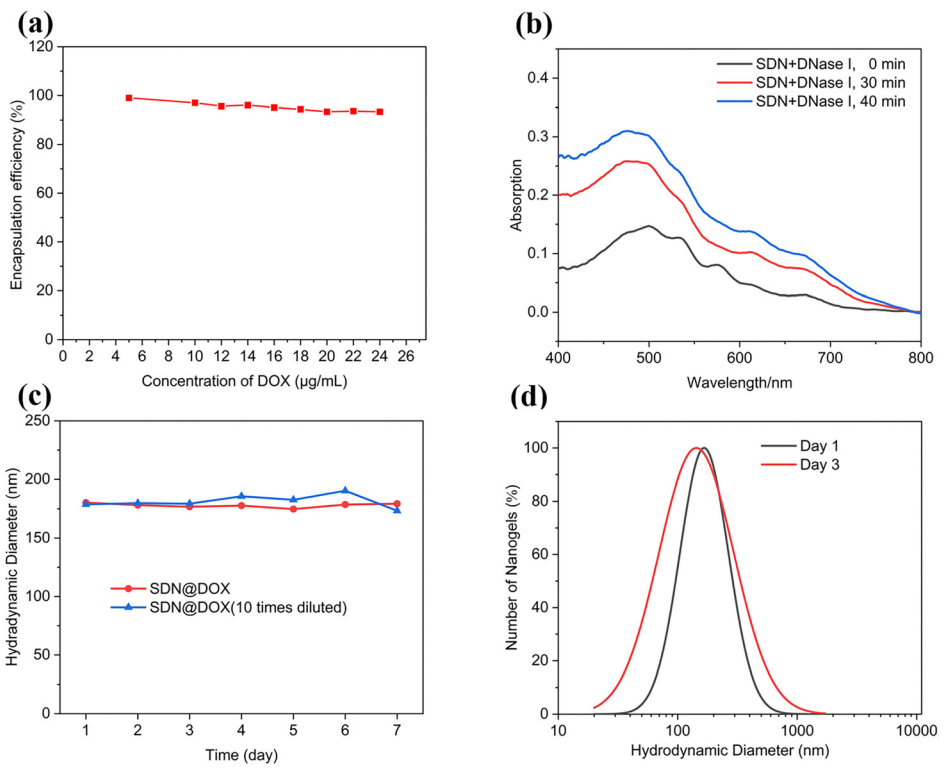

Fig. 3 (a) The drug loading rate of SDN co-incubated with different concentrations of DOX; (b) DOX release of SDN@DOX after treating with DNase I (50 U mL^{-1}); (c) DLS changes of SDN@DOX in PBS for 7 days; (d) DLS changes of SDN@DOX in DMEM with 10% serum for 3 days.

and the size was continuously observed by DLS and TEM (Fig. 3c and Fig. S9). It showed that SDN@DOX maintained the size of 170 nm over 7 days. Even after 10-fold dilution, the nanogel size remained unchanged. Additionally, the nanogel was incubated in DMEM medium containing 10% fetal bovine serum for one day and 3 days respectively (Fig. 3d). The nanogel remained stable. These results confirmed the excellent stability of the dual-drug loaded supramolecular DNA nanogel in a physiologically relevant environment.

Cell uptake and intracellular ROS generation

Spermine is overexpressed in patients with breast cancer.[46–48] Therefore, MCF-7 cells (human breast cancer epithelial cells), 4T1 cells (murine triple-negative breast cancer cells) and 3T3 cells (normal cells as control) were selected for subsequent cell experiments. Firstly, MCF-7 cells were used as a model to choose the concentration ratio of MB and Dox for the SDN@DOX system. The cytotoxicity assays were conducted to determine the optimal drug concentration ratio by varying the proportion of DOX while maintaining MB at a constant concentration of 3 μM. As shown in Fig. S10, the cell viability reduced with the increasing concentration of DOX. When the $C_{DOX}:C_{MB}$ ratio reached 2 : 1, the MCF-7 cell viability dropped to approximately 20% under 660 nm light irradiation for 1 min. Therefore, a $C_{DOX}:C_{MB}$ ratio of 2 : 1 was selected for subsequent cellular studies.

Then, the cellular uptake behavior of SDN was investigated. Y-1MB-2FAM, which was composed of ssDNA1-MB, ssDNA2-FAM and ssDNA3-FAM through DNA hybridization, was utilized as a substitute for Y-1MB and combined with Y-3MB to obtain SDN-2FAM. Flow cytometry was employed to examine the cellular uptake. As compared to Y-dsDNA-1MB-2FAM, the formation of SDN-2FAM resulted in a substantial increase in FAM signal intensity within MCF-7 cells, with the cellular uptake of SDN-2FAM being about tenfold higher (Fig. 4a). This trend was consistently observed in the uptake experiments of 4T1 cells (Fig. S11). In the 3T3 cell system, the intensity of SDN was higher than that of Y-DNA but was significantly lower than that in the cancer cell system including MCF-7 and 4T1. These results suggest that the design of nanostructures has a

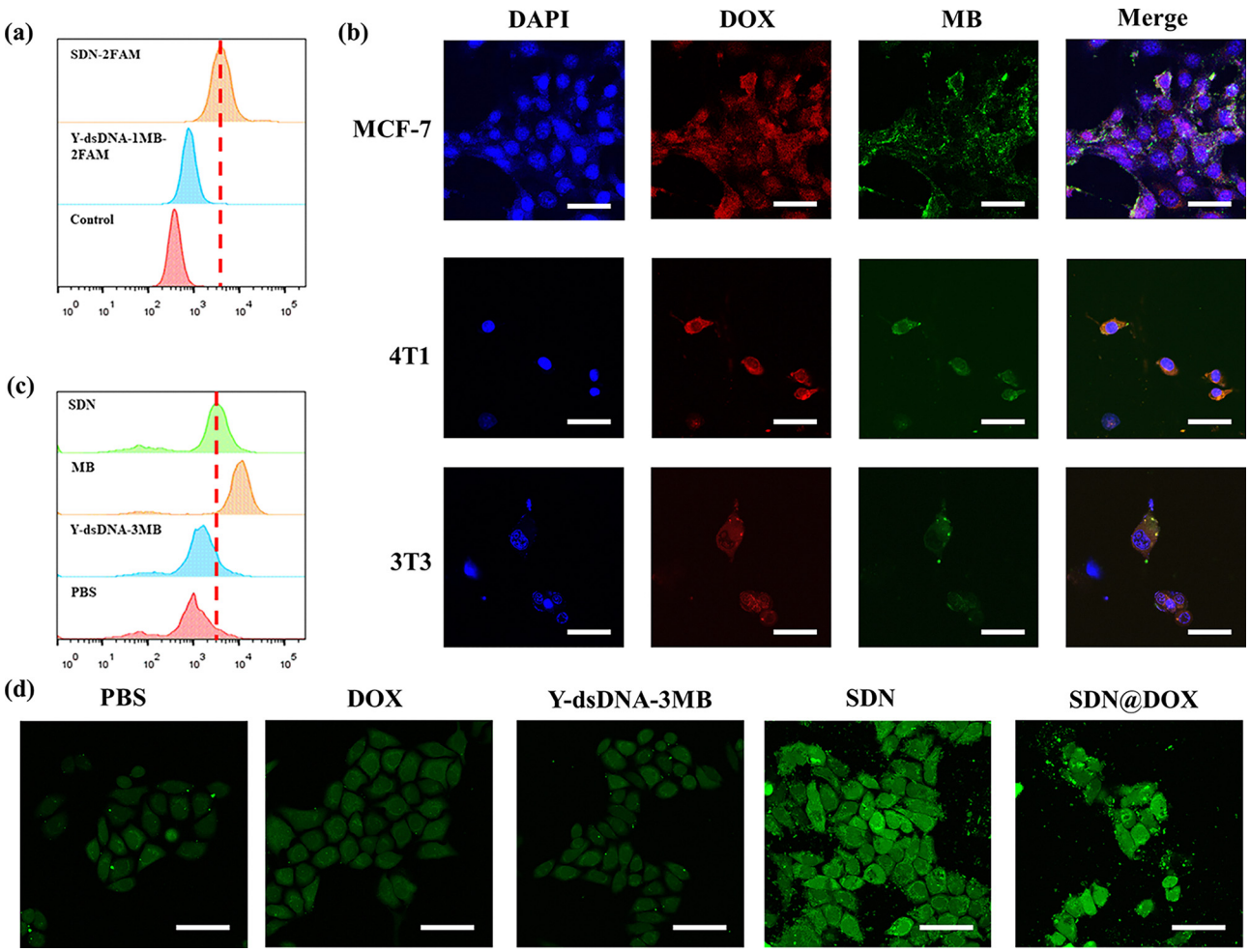

Fig. 4 (a) Flow cytometry analysis of SDN-2FAM uptake by MCF-7 cells; (b) CLSM images showing the cellular uptake of SDN@DOX in MCF-7, 4T1, and 3T3 cells; (c) flow cytometry analysis of intracellular ROS generation in MCF-7 cells; (d) CLSM images illustrating intracellular ROS generation in MCF-7 cells (scale bar: 50 μm).

significant impact on cellular uptake efficiency. As established in the literature for DNA-based nanomaterials,[50,51] their cellular uptake is primarily mediated by the clathrin and micropinocytosis-dependent endocytic pathway. Studies indicate that DNA nanogels typically reach late endosomes or lysosomes and then achieve lysosomal escape, a process potentially facilitated by the intrinsic physicochemical properties of DNA itself, even in the absence of specialized structural designs. Given that our system is a supramolecular DNA nanogel constructed *via* host–guest recognition and is fundamentally assembled through non-covalent bonds, it is reasonable to hypothesize that it follows these same fundamental trafficking principles.

To further evaluate the drug delivery capacity of SDN, we detected the fluorescence signals of DOX and MB molecules in different cell lines. As shown in Fig. 4b, obvious fluorescence signals of DOX and MB were observed in MCF-7, 4T1 and 3T3 cells, indicating that SDN could effectively deliver drugs into cells. Flow cytometry results showed that the uptake efficiency of SDN@DOX by MCF-7 and 4T1 cancer cells was close to that of the free DOX group, while the uptake level of 3T3 normal cells was relatively low (Fig. S12). This difference may be related to the lower metabolic activity of 3T3 cells. To further verify the photodynamic therapeutic effect of SDN, we used the DCFH-DA probe to detect the intracellular reactive oxygen species (ROS) level. As shown in Fig. 4c, after co-incubation of CF-7 cells with SDN for 6 hours, the ROS generation level in the SDN group was lower than that in the MB alone treatment group, but significantly higher than that in the PBS group and the Y-dsDNA-3MB group. This result was consistent with the cell uptake experiment and further supported the high efficiency of SDN in drug delivery. A similar trend was also observed in 4T1 cells (Fig. S13a). However, in the 3T3 cell experimental group (Fig. S13b), the difference in ROS generation levels was not as obvious as in the tumor cell experimental groups. Although the uptake of SDN by 3T3 cells was significantly higher than that of the Y-3MB group, the lower spermine level in 3T3 cells prevented the MB carried by SDN from fully exerting its ability to generate ROS in 3T3 cells. The above results indicated that the photodynamic therapeutic effect of SDN was related to the cell uptake ability and intracellular spermine expression level, verifying the effectiveness of the supramolecular therapeutic strategy. Confocal laser scanning microscopy (CLSM) images visually demonstrated the differences in ROS generation intensity among the groups of MCF-7 and 4T1 cells (Fig. 4d and Fig. S14).

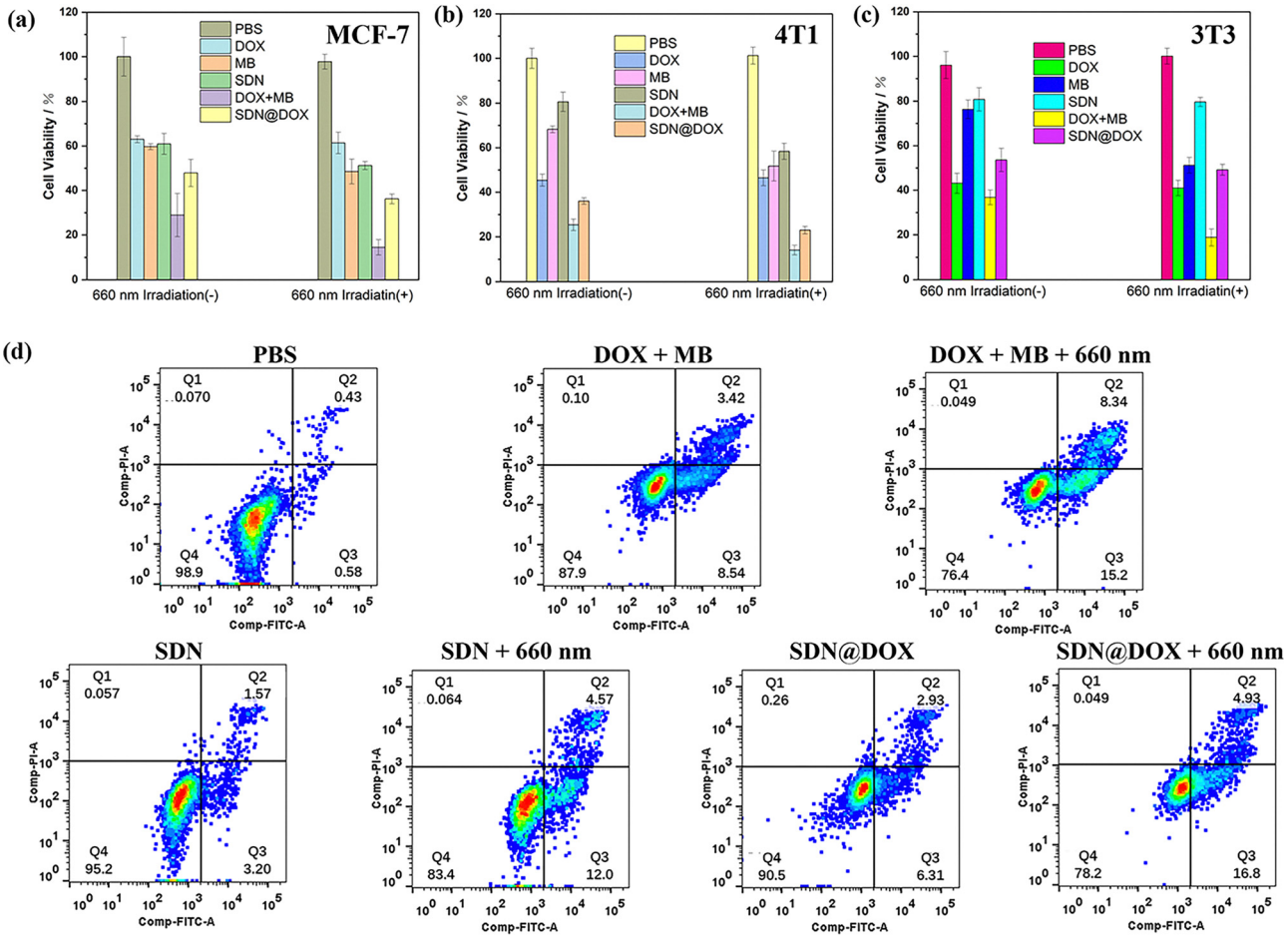

Fig. 5 (a)–(c) Evaluation of cytotoxicity following co-incubation of MCF-7 cells, 4T1 cells, and 3T3 cells with DOX, MB, SDN, DOX + MB, and SDN@DOX; (d) cell apoptosis levels of MCF-7 cells after incubation with different samples by flow cytometric analysis.

Anticancer activity of SDN@DOX

Given the different uptake behaviors of the above-mentioned cells towards SDN, we further investigated their combined therapeutic effects. As shown in Fig. 5a and b, in MCF-7 and 4T1 cells, SDN demonstrated photodynamic therapeutic effects comparable to those of MB. Additionally, after loading DOX, the therapeutic effects of the SDN@DOX were superior to those of SDN or DOX alone in both cell lines. Compared with the free dual-drug group, the cytotoxic effect of SDN@DOX on MCF-7 cells was slightly lower than that on 4T1 cells, possibly due to the lower uptake of SDN@DOX by MCF-7 cells. In the 3T3 cell group (Fig. 5c), MB exhibited significant photodynamic therapeutic activity, while the SDN group only showed weak photodynamic effects, mainly reflecting the dark toxicity of MB. Moreover, the combined therapeutic effect of the SDN@DOX group was not significant, and the therapeutic effect was mainly attributed to the DOX loaded on SDN. To further verify these results, we conducted apoptosis detection using Annexin V-FITC/PI staining. As shown in Fig. 5d and Fig. S15, the analysis of the apoptosis detection results on MCF-7 cells indicates that after light exposure, the apoptosis rates of the MB + DOX group, the SDN group, and the SDN@DOX group all significantly increased, with an overall increase of more than 10%. This result suggests that light can effectively activate the photodynamic therapy effects of these treatment groups, thereby inducing apoptosis in tumor cells. Additionally, experiments on 4T1 cells also showed a similar trend (Fig. S16 and S17), especially after light exposure, the apoptosis degree of the SDN@DOX group was significantly higher than that of the SDN group, indicating that the introduction of DOX enhanced the therapeutic effect to a certain extent, which is related to its synergistic effect. However, the results in 3T3 cells were different (Fig. S18 and S19). Whether it was the SDN group or the SDN@DOX group, the induction of apoptosis in 3T3 cells before and after light exposure was very limited and almost negligible. This indicates that MB in the SDN@DOX system in normal cells is in a relatively inert state. Additionally, after light exposure, the apoptosis rate (early apoptosis + late apoptosis) of the SDN group in MCF-7 cells increased by 11.8% (8.55% in 4T1 cells and 2.73% in 3T3 cells). In the SDN@DOX group, the corresponding apoptosis growth rates of the three groups of cells were 12.49%, 19.74%, and 1.51%, respectively. This result suggests that light can effectively activate the photodynamic therapy effects of these treatment groups in tumor cells, thereby inducing apoptosis in tumor cells. In summary, the experimental results not only verify the effectiveness of light in activating the SDN and SDN@DOX systems but also demonstrate the positive role of DOX in enhancing the therapeutic effect. At the same time, it reveals the good biological safety of this system towards normal cells, highlighting its potential application value in tumor photodynamic therapy.

Conclusion

In this study, we integrated a supramolecular therapeutic system with a DNA self-assembly system to successfully develop a supramolecular DNA nanogel, which combines both supramolecular photodynamic therapy and chemotherapy effects. In addition to the demonstrated advantages of controllable size, stability, and stimulus-responsive drug release, SDN has significant potential for further exploration. Firstly, this design offers high flexibility, the guest molecules can be readily replaced, and it is feasible to conjugate more functional guest molecules to DNA through synthesis. Secondly, although we have only preliminarily harnessed the programmable nature of DNA without fully exploring its advanced functions such as targeting, therapeutic efficacy, and stimulus responsiveness, advancements in supramolecular chemistry and DNA nanotechnology are expected to enable the design of more complex and multifunctional SDNs in the future, thereby meeting diverse diagnostic and therapeutic needs.

Materials and methods

Materials

All the DNA sequences were sourced from Hippobio (Zhejiang, China). The water used in all experiments was Milli-Q deionized water (18.2 MΩ cm). The DCFH utilized for *in vitro* experiments was obtained through the reaction of DCFH-DA (2,7-dichlorodihydrofluorescein diacetate) with NaOH.

The size and morphology were determined by DLS (PSS, USA), TEM (JEOL, USA), UlV-vis spectrophotometry (UV-3600, shimadzu, Japan), fluorescence spectrophotometry (LS 55, PerkinElmer, UK), and flow cytometry (FACS Celesta, BD/Becton Dickinson, US).

Preparation of Y-shaped building units and SDN

All DNA assembly procedures were conducted in TM buffer (20 mM Tris, 10 mM $MgCl_2$, pH = 7.4). The concentration of the CB[8] is 10 μM, dissolved in TM buffer. The detailed procedural steps are as follows:

Y-dsDNA-3MB (Y-3MB) is composed of ssDNA1-MB, ssDNA2-MB and ssDNA3-MB. Y-dsDNA-1MB (Y-1M) is composed of ssDNA1-MB, ssDNA2 and ssDNA3. Y-dsDNA-1MB-2FAM is composed of ssDNA1-MB, ssDNA2-FAM and ssDNA3-FAM. In the preparation of Y-3MB, 30 μL of each of ssDNA1-MB, ssDNA2-MB, and ssDNA3-MB solutions at a concentration of 90 μM were individually measured and combined. The mixture was then subjected to vigorous shaking to ensure complete homogenization. Subsequently, it was heated to 90 °C for 5 min, and then gradually cooled to room temperature to obtain Y-3MB. The remaining Y-shaped building units were prepared using the identical method. All Y-shaped building units are used immediately upon assembly.

The assembly concentrations of SDN are detailed in Table S2. In detail, 30 μL of Y-3MB solution (30 μM) and 10 μL of Y-1MB solution (30 μM) were carefully measured and mixed thoroughly. Subsequently, 300 μL of CB[8] solution (10 μM) and 660 μL of TM buffer solution were added. The mixture was then vigorously shaken to ensure complete homogenization, followed by sonication for 3 minutes. Subsequently, the mixture

was incubated at room temperature for 24 h, during which it was shaken every 2–3 hours, resulting in the formation of SDN.

Guest molecule competition experiment

FGG peptides competitive binding assay. Accurately measure 1 mL of the prepared SDN solution (C_{MB} = 3 μM), vortex to ensure uniformity, and aliquot into 10 equal portions, each containing 100 μL. Sequentially add 0, 0.1, 0.5, 1, 2, 5, 10 and 20 μL of a 3 mM FGG peptides aqueous solution to each portion. Adjust the final volume of each sample to 120 μL with deionized water and mix thoroughly. Incubate the samples at 37 °C for 1 h. Subsequently, analyze the changes in the ultraviolet absorption spectra of the samples.

Spermine competitive binding assay. This step follows a similar procedure to the preceding one. Accurately measure 1 mL of the prepared SDN solution (C_{MB} = 3 μM)., vortex to ensure uniformity, and aliquot into 10 equal portions, each containing 100 μL. Different volumes of spermine aqueous solution were added to the samples, after which the volume of each sample was adjusted to 120 μL with deionized water. This ensured that the final spermine concentrations in the samples were 3, 15, 30, 60, 150, 300, 600, 3000 and 6000 μM, respectively. Incubate the samples at 37 °C for 1 h. Subsequently, analyze the changes in the ultraviolet absorption spectra of the samples.

In vitro detection of ROS

DCFH was used as a reagent for ROS detection *in vitro*. Add 5 μL DCFH solution (20 μM) to 100 μL SDN solution (C_{MB} = 3 μM). After the mixture was evenly mixed, the fluorescence intensity at 525 nm was recorded by irradiation at 660 nm (60 mW cm^{-2}) for different times (0–120 s) to evaluate the ROS generation ability. The same processing steps are applied to other samples.

The loading and release of DOX

During the preparation of SDN, it was co-incubated with a series of DOX solutions at varying concentrations. After 24 hours of incubation, the mixture was subjected to high-speed centrifugation to obtain SDN@DOX. The supernatant was collected, and the fluorescence intensity of DOX at 590 nm was measured. The concentration of unbound DOX in the supernatant was calculated using the linear regression equation $F = 27.583C + 4.4808$. Finally, the loading efficiency of DOX by SDN under different initial DOX concentrations was determined.

The conditions for treating SDN@DOX with DNase I were as follows: 40 mM Tris–HCl, 1 mM $CaCl_2$, 10 mM $MgCl_2$, PH = 7.5; C_{DOX} = 10 μg mL^{-1}, C_{DNA} = 32.67 μg mL^{-1}, and $C_{DNase\,I}$ = 50 U mL^{-1}.

Cell culture

MCF-7 cells and 3T3 cells were cultured in Dulbecco's modified Eagle's medium (DMEM, Gibco, USA) containing 10% FBS and 1% penicillin/streptomycin at 37 °C and 5% CO_2.

4T1 cells were cultured in RMPI medium 1640 containing 10% FBS and 1% penicillin/streptomycin at 37 °C and 5% CO_2.

Intracellular ROS generation

DCFH-DA was utilized as a sensor for detecting intracellular ROS generation. After the cells were incubated under standard conditions for 24 h, they were further incubated with the sample group for 6 h. Except for the blank control group which received no treatment, the concentrations of MB in the other sample groups were all 3 μM. After the incubation, cells were washed thoroughly with PBS. Subsequently, cells were stained with a medium containing 5 μM DCFH-DA for 15 minutes. After staining, cells were exposed to 660 nm light (60 mW cm^{-2}) for 2 min and then analyzed using CLSM and flow cytometry to assess intracellular ROS levels.

Cytotoxicity assay

The cell cytotoxicity of each sample group was assessed using the MTT assay. Cells were seeded in 96-well plates and incubated under standard conditions for 24 h. The old culture medium was then aspirated, and fresh medium containing the respective samples was added for an additional 24-hour incubation. Following this, the medium was replaced with fresh culture medium, and cells were exposed to 660 nm light (60 mW cm^{-2}) for 2 min, followed by a further 24-hour incubation. After the incubation period, MTT reagent was added to each well and incubated for 4 h. Subsequently, the medium was aspirated, and 150 μL of DMSO was added to each well to dissolve the formazan crystals. Absorbance was measured using a microplate reader at 492 nm to determine the final results.

Cell apoptosis assay

Cell apoptosis was assessed using the Annexin V-FITC/PI apoptosis detection kit. Cells were seeded in 6-well plates and incubated for 24 h. The old culture medium was then aspirated, and fresh medium containing the respective samples was added for an additional 12-hour incubation. Following this, the medium was replaced with fresh culture medium, and cells were exposed to 660 nm light (60 mW cm^{-2}) for 2 min, followed by a further 12-hour incubation. Subsequently, the cells were digested with trypsin and washed 3 times with PBS. The collected cells were stained with Annexin V-FITC/PI apoptosis kit for 30 min, then analyzed by flow cytometry.

Author contributions

Z. D.: methodology, investigation, formal analysis, writing – original draft. X. Y.: methodology, investigation. P. J.: methodology. S. W.: methodology. J. C.: methodology. Z. Z.: conceptualization, writing – review and editing, supervision, funding acquisition. S. L.: conceptualization, supervision, funding acquisition.

Zongze Duan: formal analysis (lead), investigation (lead), methodology (lead), writing – original draft (lead); Xiang Yu: investigation (supporting), methodology (supporting); Pengwei Jiang: methodology (supporting); Shuhao Wang: methodology (supporting); Junling Chen: methodology (supporting); Zhiyong

Zhao: conceptualization (lead), funding acquisition (equal), investigation (supporting) project administration (lead), supervision (lead), writing – review & editing (lead); Simin Liu: conceptualization (supporting), funding acquisition (equal), supervision (supporting).

Conflicts of interest

There are no conflicts to declare.

Data availability

The data supporting this article have been included as part of the supplementary information (SI). Supplementary information is available. See DOI: **https://doi.org/10.1039/d5nh00588d**.

Acknowledgements

This work was financially supported by the National Natural Science Foundation of China (No. 21604066 and 21871216).

Notes and references

1 *Nat. Cancer*, 2021, **2**, 245–246.
2 L. Huang, S. Zhao, J. Wu, L. Yu, N. Singh, K. Yang, M. Lan, P. Wang and J. S. Kim, *Coord. Chem. Rev.*, 2021, **438**, 213888.
3 H. S. Jung, P. Verwilst, A. Sharma, J. Shin, J. L. Sessler and J. S. Kima, *Chem. Soc. Rev.*, 2018, **47**, 2280–2297.
4 Z. Tang, P. Zhao, H. Wang, Y. Liu and W. Bu, *Chem. Rev.*, 2021, **121**, 1981–2019.
5 Y.-F. Ding, X. Xu, J. Li, Z. Wang, J. Luo, G. S. P. Mok, S. Li and R. Wang, *Acta Biomater.*, 2023, **164**, 397–406.
6 Z. Zhou, B. Edil and M. Li, *BMC Med.*, 2023, **21**, 171.
7 K. Yang, B. Hua, S. Qi, B. Bai, C. Yu, F. Huang and G. Yu, *Angew. Chem., Int. Ed.*, 2022, **61**, e202213572.
8 F. Lu, J. Wang, C. Tao and J.-J. Zhu, *Nanoscale Horiz.*, 2018, **3**, 538–544.
9 K. Yu, X. Hai, S. Yue, W. Song and S. Bi, *Chem. Eng. J.*, 2021, **419**, 129535.
10 Y. Opoku-Damoah, R. Zhang, H. T. Ta and Z. P. Xu, *Biomater. Sci.*, 2021, **9**, 6086–6097.
11 J. Wang, Q. Zhou, X. Li, D. Dutta and Z. Ge, *ACS Macro Lett.*, 2022, **11**, 543–548.
12 R. Xu, E. Zhu, X. Lan, Q. Yang and C. Zhang, *Smart Mater. Med.*, 2024, **5**, 373–385.
13 Y. Qin, L. Yang, Y. Yang, W. Gao, K. Aihemaiti, G. Jiang, R. Huang, H. Khan and R. Huang, *J. Controlled Release*, 2024, **376**, 542–552.
14 P. Gupta, H. Kaur, M. Anees, S. Tiwari, A. Bansal and H. Singh, *Nanoscale Horiz.*, 2025, **10**, 1465–1477.
15 A. Nain, Y.-T. Tseng, A. Gupta, Y.-F. Lin, S. Arumugam, Y.-F. Huang, C.-C. Huang and H.-T. Chang, *Nanoscale Horiz.*, 2023, **8**, 1652–1664.
16 Z. Yan, Z. Duan, S. Liu and Z. Zhao, *Biomacromolecules*, 2024, **25**, 7123–7133.
17 Q. Hu, H. Li, L. Wang, H. Gu and C. Fan, *Chem. Rev.*, 2019, **119**, 6459–6506.
18 M. M. C. Bastings, F. M. Anastassaco, N. Ponnuswam, F. G. Leifer, G. Cuneo, C. Lin, D. E. Ingber, J. H. Ryu and W. M. Shih, *Nano Lett.*, 2018, **18**, 3557–3564.
19 A. Lacroix and H. F. Sleiman, *ACS Nano*, 2021, **15**, 3631–3645.
20 H. Ji and Q. Zhu, *J. Controlled Release*, 2023, **361**, 803–818.
21 P. W. K. Rothemund, *Nature*, 2006, **440**, 297–302.
22 B. Wei, M. Dai and P. Yin, *Nature*, 2012, **485**, 623–626.
23 Q. Jiang, Y. Shang, Y. Xie and B. Ding, *Adv. Mater.*, 2024, **36**, 2301035.
24 Y. Dong, C. Yao, Y. Zhu, L. Yang, D. Luo and D. Yang, *Chem. Rev.*, 2020, **120**, 9420–9481.
25 Y. Peng, Z. Gao, B. Qiao, D. Li, H. Pang, X. Lai, Q. Pu, R. Zhang, X. Zhao, G. Zhao, D. Xu, Y. Wang, Y. Ji, H. Pei and Q. Wu, *Adv. Sci.*, 2023, **10**, 2300614.
26 N. Jain, A. Singh and D. Bhatia, *Nanoscale*, 2025, **17**, 18–52.
27 G. Pan, Q. Mou, Y. Ma, F. Ding, J. Zhan, Y. Guo, X. Huang, Q. Li, X. Zhu and C. Zhang, *ACS Appl. Mater. Interfaces*, 2019, **11**, 41082–41090.
28 F. Li, J. Tang, J. Geng, D. Luo and D. Yang, *Prog. Polym. Sci.*, 2019, **98**, 101163–101187.
29 J. Zhang, Y. Guo, G. Pan, P. Wang, Y. Li, X. Zhu and C. Zhang, *ACS Appl. Mater. Interfaces*, 2020, **12**, 21441–21449.
30 X. Gao, S. Li, F. Ding, X. Liu, Y. Wu, J. Li, J. Feng, X. Zhu and C. Zhang, *Adv. Mater.*, 2021, **33**, 2006116.
31 Y. Yong and C. Fan, *Chem*, 2022, **8**, 1554–1566.
32 M. Yan, S. Wu, Y. Wang, M. Liang, M. Wang, W. Hu, G. Yu, Z. Mao, F. Huang and J. Zhou, *Adv. Mater.*, 2024, **36**, 2304249.
33 B. Hazarika and V. P. Singh, *Chin. Chem. Lett.*, 2023, **34**, 108220–108237.
34 Y.-Y. Liu, X.-Y. Yu, Y.-C. Pan, H. Yin, S. Chao, Y. Li, H. Ma, M. Zuo, K.-X. Teng, J.-L. Hou, Y. Chen, D.-S. Guo, R. Wang, Y. Pei, Z. Pei, J.-F. Xu, X.-Y. Hu, C. Li, Q.-Z. Yang, L. Wang, Y. Liu and Z.-T. Li, *Sci. China: Chem.*, 2024, **67**, 1397–1441.
35 S. J. Barrow, S. Kasera, M. J. Rowland, J. D. Barrio and O. A. Scherman, *Chem. Rev.*, 2016, **116**, 12651–12652.
36 H. Yin and R. Wang, *Isr. J. Chem.*, 2018, **58**, 188–198.
37 L. Armstrong, S. L. Chang, N. Clements, Z. Hirani, L. B. Kimberly, K. Odoi-Adams, P. Suating, H. F. Taylor, S. A. Trauth and A. R. Urbach, *Chem. Soc. Rev.*, 2024, **53**, 11519–11556.
38 J. A. Plumb, B. Venugopal, R. Oun, N. Gomez-Roman, Y. Kawazoe, N. S. Venkataramanan and N. J. Wheate, *Metallomics*, 2012, **4**, 561–567.
39 Y. Chen, Z. Huang, H. Zhao, J.-F. Xu, Z. Sun and X. Zhang, *ACS Appl. Mater. Interfaces*, 2017, **9**, 8602–8608.
40 D. Wu, J. Wang, X. Du, Y. Cao, K. Ping and D. Liu, *J. Nanobiotechnol.*, 2024, **22**, 235.
41 W. Wang, B. Qi, X. Yu, W.-Z. Li, Z. Yang, H. Zhang, S. Liu, Y. Liu and X.-Q. Wang, *Adv. Funct. Mater.*, 2020, **30**, 2004452.
42 P. Paul and G. S. Kumar, *Spectrochim. Acta, Part A*, 2013, **107**, 303–310.
43 P. Montes-Navajas, A. Corma and H. Garcia, *ChemPhysChem*, 2008, **9**, 713–720.
44 F. Li, Y. Q. Xu, H. Li, C. Wang, A. Lu and S. Sun, *New J. Chem.*, 2014, **38**, 1396–1400.

45 J. M. Chinai, A. B. Taylor, L. M. Ryno, N. D. Hargreaves, C. A. Morris, P. J. Hart and A. R. Urbach, *J. Am. Chem. Soc.*, 2011, **133**, 8810–8813.
46 J. Levêque, F. Foucher, J. Y. Bansard, R. Havouis, J. Y. Grall and J. P. Moulinoux, *Breast Cancer Res. Treat.*, 2000, **60**, 99–105.
47 E. W. Gerner and F. L. Meyskens, *Nat. Rev. Cancer*, 2004, **4**, 781–792.
48 B. Xi, H. Zha, Y.-F. Din, Z. Wang, Y. Wan, C. Ga and R. Wang, *J. Controlled Release*, 2023, **357**, 572–579.
49 Z. Duan, G. Dong, H. Yang, Z. Yan, S. Liu, Y. Dong and Z. Zhao, *J. Mater. Chem. B*, 2024, **12**, 6137–6145.
50 J. Wang, J. Li, Y. Chen, R. Liu, Y. Wu, J. Liu, X. Yang, K. Wang and J. Huang, *Nano Lett.*, 2022, **22**, 8216–8223.
51 J. Wu, X. Zheng, W. Lin, L. Chen and Z.-S. Wu, *Adv. Healthcare Mater.*, 2024, **13**, 2303865.